JOURNAL OF GEOPHYSICAL RESEARCH, VOL. 108, NO. C2, 3032, doi:10.1029/2001JC000903, 2003

A comparison between radar imagery and coupled wave-current model results for a study of northwest Pacific seamount trapped waves

R.-Q. Lin
Department of Seakeeping, David Taylor Model Basin, Carderock, West Bethesda, MD, USA

S. R. Chubb
Remote Sensing Division, Naval Research Laboratory, Washington, D. C., USA

Received 5 April 2001; revised 20 June 2002; accepted 23 July 2002; published 13 February 2003.

[1] This paper demonstrates that a coupled new coastal wave model [*Lin and Huang*, 1996a, 1996b; *Lin and Perrie*, 1997, 1999] combined with a coastal current circulation model [*Haidvogel and Aike*, 1999], accurately predicts the surface features of seamount trapped waves. The environmental conditions, such as wind, buoyancy frequency, bottom topography, latitude, and tidal current are the model-input parameters. We have tested the applicability of the coupled model, using a set of trapped waves in the vicinity of two seamounts in the Northwest Pacific ocean. Our motivation for doing this is to see if it is possible to understand the origin of sea surface manifestations of these seamounts that appear to be present in images derived using a synthetic aperture radar (SAR), from the Russian Kosmos 1870 satellite. Each seamount is about 0.7 km in height and has a 20 km semidiameter width, and the ocean is about 5 km in depth. The model results suggest it is possible to detect these kinds of sea surface signatures from even such small seamounts in deep ocean by radar imagery, directly, at low wind speeds (<1 m/s), and indirectly, at higher wind speeds, from wave-breaking that occurs in the shorter wavelength portions of the spectrum. *INDEX TERMS:* 1635 Global Change: Oceans (4203); 1640 Global Change: Remote sensing; 4572 Oceanography: Physical: Upper ocean processes; *KEYWORDS:* coupled wave-current model, radar image, seamount-trapped waves, SAR, detect ability

Citation: Lin, R.-Q., and S. R. Chubb, A comparison between radar imagery and coupled wave-current model results for a study of northwest Pacific seamount trapped waves, *J. Geophys. Res.*, *108*(C2), 3032, doi:10.1029/2001JC000903, 2003.

1. Introduction

[2] Seamount-trapped waves, resulting from the effects of sea bottom topography on incident currents, are common phenomena. When a tidal current frequency is sufficiently close to the free-wave frequency, an unexpectedly large tidal current can be generated over the top of the topographic features [*Chapman*, 1989]. This phenomenon has attracted considerable interest.

[3] Many theoretical and numerical studies on seamount trapped waves have been carried out in many previous papers. For example, *Brink* [1988] examined the effect of stratification on bottom-trapped waves. *Chapman* [1989] studied the intensification of subinertial diurnal tides over isolated seamounts. Although these studies have been based on a linear barotropic system, their conclusions seem to be applicable to more general cases. Recently, *Zhang and Boyer* [1991] studied the flow over two seamounts in a rotating and linearly stratified laboratory experiment. According to their experimental results, flow patterns vary greatly with the normalized distance between the seamounts and the incident angle of the incoming current with respect to the common axis of the seamounts.

[4] Based on work on tidally-generated internal waves near the edge of the continental shelf off New York [*Gasparovic et al.*, 1988], it was felt very unlikely that such low, deep seamounts could generate detectable signals. In particular, it was known that strain rates in excess of perhaps 5×10^{-4}/s would be required in order to render a subsurface object visible to normal synthetic aperture radars. It seemed highly unlikely to U.S. scientists that such deep features, as reported by *Chelomei et al.* [1990] could possess surface signatures detectable to current SAR or RAR systems. Nevertheless, preliminary Russian work had indicated that this could indeed be the case.

[5] We were motivated by the observation by *Chelomei et al.* [1990] of readily detectable variations in W-Band (10 cm wavelength) radar image intensity, directly over large seamounts, located several thousand meters below the sea surface, near the Kamchatka Peninsula. These sea surface manifestations of seamounts are clearly visible in one particular, high (17 m × 30 m) resolution Synthetic Aperture Radar (SAR) image [*Chelomei et al.*, 1990, Figure 3].

0148-0227/03/2001JC000903$09.00

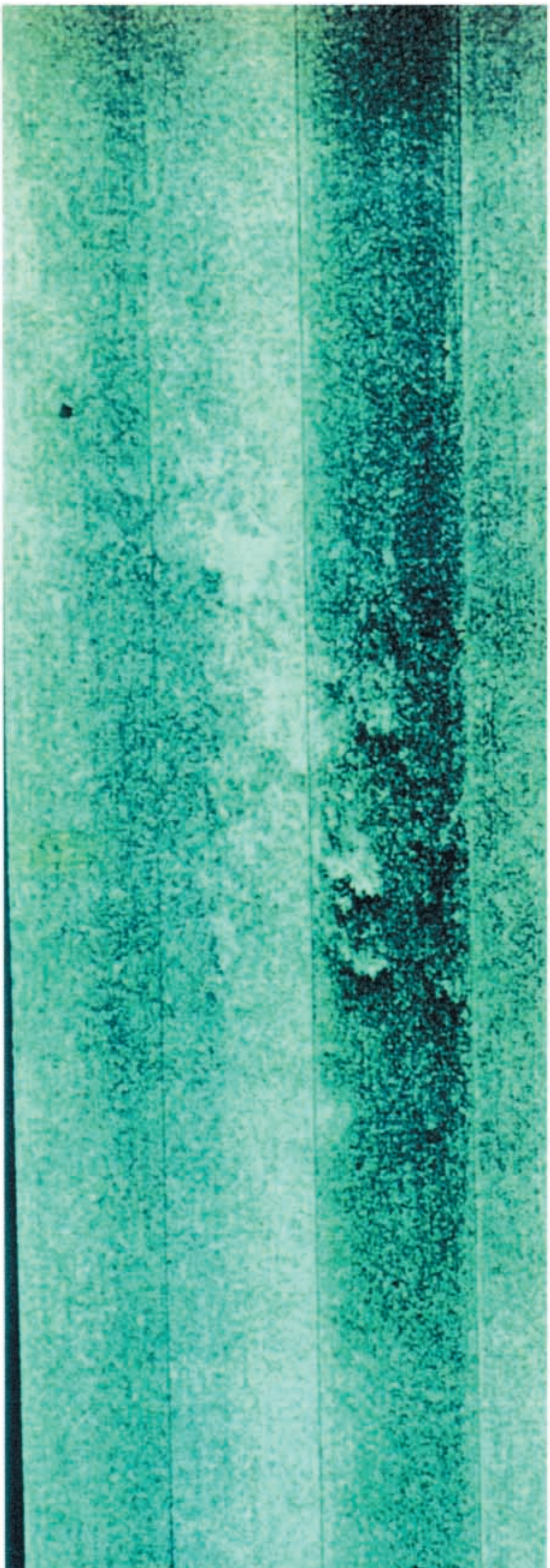

Chelomei et al. [1990] published this image in a Russian journal. Although their paper has been translated, the associated publication is not readily accessible. For this reason, these authors have provided us with a copy of the image, which we are including in Figure 1.

[6] This image was synthesized from data collected by the Satellite ''Kosmos-1870.'' Because the associated SAR image was processed using optical (as opposed to digital) techniques, it is not possible to use this image quantitatively to extract variations in image intensity, although within limits, relative variations within the image scene can be used to identify prominent changes in intensity. Despite these limitations, two prominent features are clearly visible, directly above the locations of two seamounts that are known to be located several thousand meters below the sea surface. In particular, as noted by *Chelomei et al.* [1990], the intensity variations in the center of the image (associated with the darkened oval-like structures and brightened, undulating, horizontal streaks) occur in regions where one expects '''leeward waves' between [the] two underwater rises'' [*Chelomei et al*., 1990]. The location of these seamounts is in the vicinity of 51°N latitude and 164°E longitude of the northwest Pacific Ocean. These seamounts are 0.7 km in elevation, 20 km wide, and 4.3 km below the ocean surface. Their bases are overlapping, and the distance between the half-height of the two seamounts is 30 km (A.V. Smirnov, personal communication).

[7] These observations raise many interesting questions about mean-flow-seamount-internal-wave-surface-wave interactions. For example, how are internal waves generated near the seamounts? Under what conditions are the waves resonant? Under what conditions can such internal waves be seen from aircraft or satellite radar images? What role do wave-current interactions have in bringing the internal waves to the sea surface? In this study, our goal is to examine the dynamical details of seamount trapped waves in the hope of answering some of these questions. To accomplish this, we use a coupled wave-current model to simulate the flow pattern and waves generated by a semi-diurnal tide incident on the two seamounts.

[8] The structural details of the flow field are resolved by using very high horizontal and vertical resolutions. A background stratification obtained from historical observations in the northwest Pacific for summer conditions is implemented in the numerical model [*Bell et al.*, 1974]. In addition, a mixing process is included in the model whenever buoyancy or shear flow instabilities occur. The numerical model is outlined in section 2, and the numerical results are presented in section 3. Here, we examine the uncoupled current model simulations first, followed by results from the coupled wave-current model. Since the laboratory experiments by *Zhang and Boyer* [1991] show that (case a) the distance between the two seamounts and (case b) the incident angle of the incoming current with respect to the common axis of the seamounts are two important parameters in controlling the flow pattern, we

Figure 1. (opposite) Synthetic aperture radar image from Kosmos-1870, showing surface manifestations of two seamounts in the northwest Pacific Ocean [from *Chelomei et al.*, 1990].

study three canonical cases. In case a, the two seamounts are well separated, while in case b, the two seamounts overlap, which more closely mimics what is observed in the northwest Pacific. In these two cases, the incident angle is taken as zero. In the third situation, the two seamounts overlap also, but here we use an incident angle of 90°. Since the seamount trapped waves are not sensitive to incident angle, cases b and c are not significantly different. For this reason, case c will not be shown in this study. In addition to the velocity patterns, we also present the strain rate pattern, which we use as a guide for inferring the variations in radar intensity modulation that may be observed in the SAR image. Finally, we draw conclusions from these numerical experiments.

2. Numerical Model

[9] We use a new coastal wave model (NCWM) [*Lin and Huang*, 1996a, 1996b; *Lin and Perrie*, 1997, 1999], coupled with an S-coordinate Primitive Equation Ocean circulation Model (SCRUM) [*Haidvogel and Aike*, 1999]. The reasons for using the NCWM are (1) because it is based on the action conservation equation (including wave action fluxes), and, as a consequence, the exact wave-current interactions; and (2) the nonlinear source function of our NCWM uses the "Reduced Integration Method" (RIA) procedure [*Lin and Perrie*, 1999], which is important because the RIA has been found to be more accurate, efficient, and reliable than existing state-of-the-art procedures [*Jensen et al.*, 1998]. The reasons for using SCRUM are (1) it employs S-coordinates, which are suitable for simulations involving both bottom topography and the surface mixing layer; and (2) this particular algorithm is well tested. A model of vertical stratification with a strong seasonal thermocline and an exponentially distributed deep buoyancy profile is adopted to be consistent with observations in the northwest Pacific Ocean.

2.1. Basic Equations

[10] NCWM

$$\frac{\partial A}{\partial t}+\frac{\partial\left(c_{gx}+u\right)A}{\partial x}+\frac{\partial\left(c_{gy}+v\right)A}{\partial y}+\frac{\partial c_{\theta}A}{\partial\theta}+\frac{\partial c_{gf}A}{\partial f}=S_{in}+S_{ds}+S_{nl}, \tag{1}$$

where A is the wave action spectral density (N/ω), N is energy density and ω is frequency, c_{gx}, c_{gy}, c_θ, and c_{gf} are group velocities for x, y, θ, and f coordinates respectively; u and v are the current components from current model output. The major source function S_{nl} is calculated by the Reduced Integration Approximation [*Lin and Perrie*, 1997, 1999].

[11] SCRUM

$$\frac{\partial u}{\partial t}+\vec{v}\cdot\nabla u-fv=\frac{\partial\phi}{\partial x}+F_u+D_u, \tag{2.1}$$

$$\frac{\partial v}{\partial t}+\vec{v}\cdot\nabla v+fu=\frac{\partial\phi}{\partial y}+F_v+D_v, \tag{2.2}$$

$$\frac{\partial T}{\partial t}+\vec{v}\cdot\nabla T=F_T+D_T, \tag{2.3}$$

$$\frac{\partial S}{\partial t}+\vec{v}\cdot\nabla S=F_S+D_S, \tag{2.4}$$

$$\frac{\partial\phi}{\partial z}=\frac{\rho g}{\rho_o}, \tag{2.5}$$

$$\frac{\partial u}{\partial x}+\frac{\partial v}{\partial y}+\frac{\partial w}{\partial z}=0. \tag{2.6}$$

Here, T is temperature, S is salinity, f is Coriolic force, ϕ is potential velocity, F is forcing, D is dissipation, and ρ is density.

[12] The vertical variability of all variables in the model, such as velocity and perturbation density are expanded in terms of Chebyshev polynomials of the first kind P_k,

$$(u,v,\rho,\Omega)=\sum_{k=0}^{N}\left[\hat{u}_k(x,y,t),\hat{v}_k(x,y,t),\hat{\rho}_k(x,y,t),\hat{\Omega}_k(x,y,t)\right]P_k(S), \tag{3}$$

where

$$P_k(S)=\begin{cases}T_o(S) & \text{if } k=0\\ T_k(S) & \text{if k is odd and } k\geq 1\\ T_k(S)+\frac{1}{k^2-1} & \text{if k is even and } k\geq 2\end{cases}$$

and $-1\leq S\leq 1$, $T_k(S)=\cos[k\cos^{-1}(S)]$, and the upper limit to the polynomial order is $N = 28$. The expansion coefficients $(\hat{u},\hat{v},\hat{\rho},\hat{\Omega})$ can be obtained by using matrix multiplications, which vectorize very well. This vertically stretched coordinate system is quite suitable for describing the strong nonlinear vertical stratification near the sea-surface because the grid-spacing may be resolved more finely near the surface and the bottom.

2.2. Boundary Conditions

[13] Boundary conditions are as follows,

Top ($z = \eta(x, y, t)$) for SCRUM only

$$\nu\frac{\partial u}{\partial z}=\tau_s^x(x,y,t),$$

$$\nu\frac{\partial v}{\partial z}=\tau_s^y(x,y,t),$$

$$\kappa_T\frac{\partial T}{\partial z}=\frac{Q_T}{\rho_o C_p}+\frac{1}{\rho_o C_p}\frac{\partial Q_T}{\partial T}\left(T-T_{ref}\right),$$

$$K_S\frac{\partial S}{\partial z}=\frac{(E-P)S}{\rho_o},$$

$$W=\frac{\partial\eta}{\partial t},$$

Bottom ($z = -h(x, y)$) for SCRUM only

$$\nu\frac{\partial u}{\partial z}=\tau_b^x(x,y,t),$$

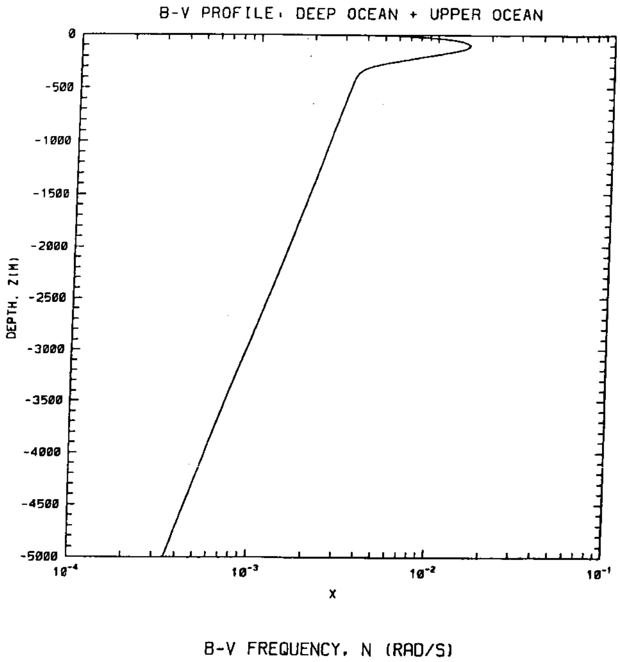

Figure 2. Vertical profile of the Brunt-Väisälä frequency observed in the northwest Pacific Ocean, [from *Bell et al.*, 1974].

$$\nu \frac{\partial v}{\partial z} = \tau_b^y(x, y, t),$$

$$\kappa_T \frac{\partial T}{\partial z} = 0.$$

$$K_S \frac{\partial S}{\partial z} = 0.$$

$$-w + \vec{v} \cdot \nabla h = 0.,$$

where τ is wind stress and w is vertical velocity.

2.3. Vertical Stratification

[14] It is well known that topographic waves in stratified oceans are generally bottom-trapped, with the wave amplitude declining rapidly upward. Since we are interested in finding out whether these waves can produce surface signatures that may be seen in radar images, nonuniform stratification is important. From the observational data, we knew that in the northwest Pacific, there is a near-surface density gradient, which is due to the seasonal thermocline, followed by a weaker permanent thermocline [*Bell et al.*, 1974]. The Brunt-Väisälä frequency (N) is then modeled by a Gaussian profile describing the near-surface buoyancy, superimposed on an exponentially decreasing deep-ocean buoyancy profile, as follows:

$$N(z) = 4.2 \exp(z/2000) + 18.4(|z|/100) \exp\{-z^2/[2(100^2)]\}.$$

A plot of N is shown in Figure 2. The Brunt-Väisälä frequency increases rapidly from 4.2 to 18.4 mrad/s within depths that are less than $\sim$100 m of the sea surface and then exponentially decreases beneath the sea surface to 0.34 mrad/s at the bottom, characteristic of the deep ocean.

2.4. Bottom Topographic Features

[15] The seamount elevation is modeled by symmetric Gaussian heights,

$$h(x, y) = h_i \exp\left[-\frac{(x - x_i)^2 + (y - y_i)^2}{d_i^2}\right],$$

where (x_i, y_i) is the location of the seamount's center, h_i is the height of the seamount, and d_i is its width. In this study, $i = 1, 2$; when $x \leq L/2$, $i = 1$, and when $x > L/2$, $i = 2$, $h_1 = h_2$ = 700 m, and $d_1 = d_2 = 10$ km (A. V. Smirnov, private communication, 1992). Figure 3 shows the two-seamount topography: Figure 3a, two seamounts far apart; and Figure 3b, two seamounts overlapped.

2.4.1. Forcing

[16] We use semidiurnal barotropic tidal forcing because it is the dominant component in the region, and the frequency of the semidiurnal tide is closer to the free-wave frequency than that of the diurnal tide. The tidal current is constrained to be parallel to the side walls. Its maximum amplitude is 0.25 m/s, and its period (T) is 12.5 hours. The semidiurnal tide is

$$u = -0.25\{1 + \tanh[(t - 6T)/(3T)]\}/2 \sin(2\pi t/T).$$

The factor inside the curly braces is used to slowly turn on the model from an initial state of rest. As we will see later, the model reaches a quasi-periodic state within approximately 10 periods. Without this spin-up factor, the sudden impact of the tidal currents may cause extremely high wave amplitudes and numerical errors.

3. Results

[17] We have carried out two sets of numerical experiments for tidal current flow over two seamounts. First we used a conventional, more traditional procedure, involving an uncoupled current model [*Haidvogel and Aike*, 1999]. Then we used a coupled wave-current model (the model by Lin et al. plus the model by Haidvogel et al.).

3.1. Results from Uncoupled Current Model

[18] In the first experiment, case a, the two seamounts are well separated and are aligned along the axis of the incoming tidal currents. In the second experiment, case b, the two seamounts overlap and are also aligned along the axis of incoming tidal currents; thus, the bottom-trapped waves around the two seamounts interact strongly. In the following discussion, we will refer to the seamount on the left as the left seamount, assuming we are looking northward. Similarly, the other seamount will be called the right seamount. Since the tidal currents come from the east for a normalized tidal current period, such as $t = 0.0-0.5$, the left seamount is downstream relative to the right one, and the right seamount is upstream. As the direction of the incident tidal current reverses for t = 0.5–1.0, the left seamount becomes the upstream seamount and the right one becomes the downstream seamount. This information is presented in two parts.

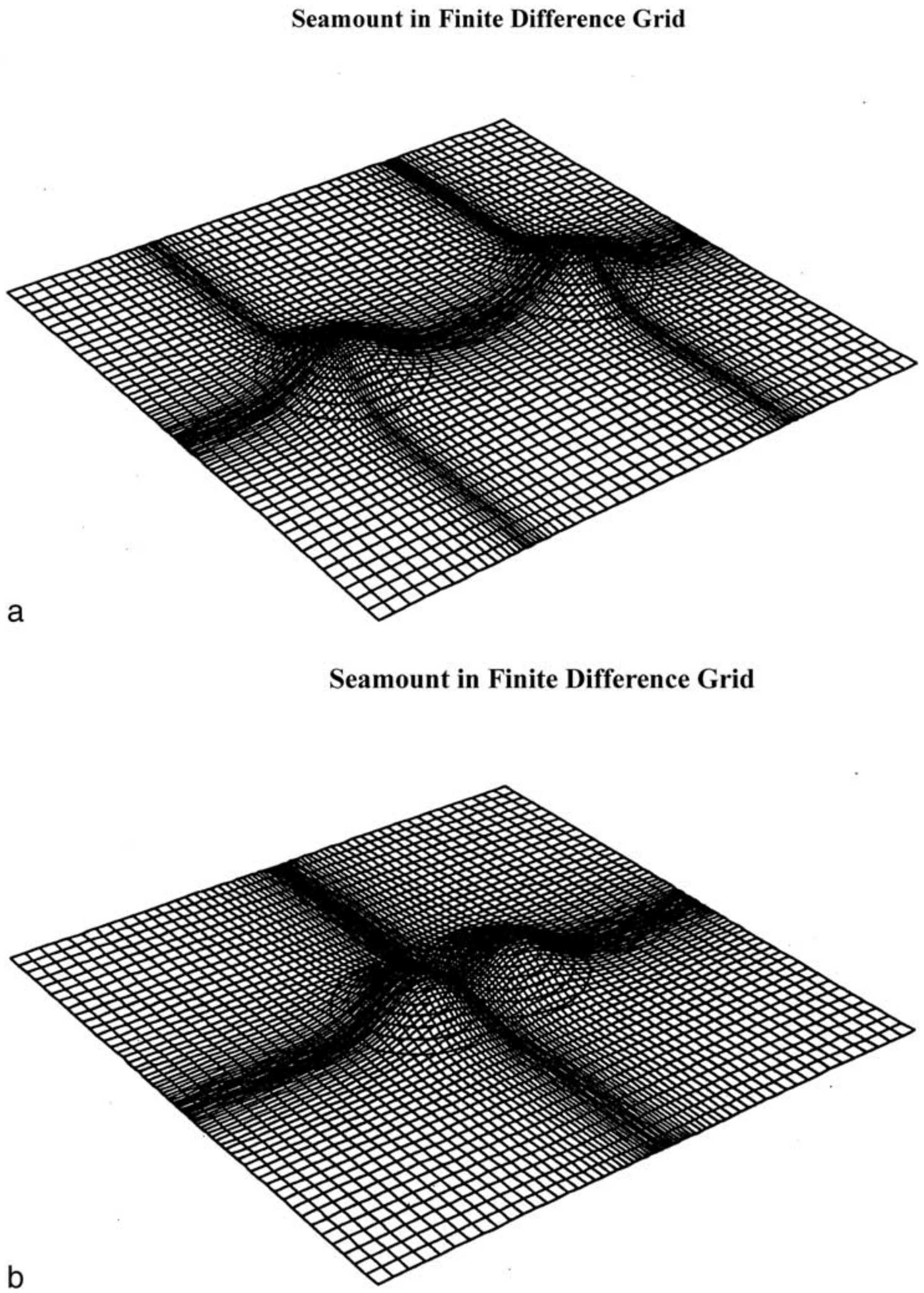

Figure 3. Topography and grid pattern. (a) A stretched grid for two seamounts that are far apart. The actual grid used in the model is twice as fine as that shown, and domain is 100 km on a side. (b) The same as Figure 3a, except the two seamounts are close to each other.

The instantaneous wave patterns are discussed first; next, the mean-flow fields are presented.

[19] Since the semidiurnal tidal forcing has a period of T (from the observational data, we know that T = 12.5 hours), the forced waves have the same period. We therefore show wave patterns for one full period. We use a nondimensional unit of time t, in which one unit is equivalent to 12.5 hours of real time. Thus, to show the wave solution, we present patterns at four times: $t = 0$, 0.25, 0.5, 0.75. It is worthwhile noting that the wave patterns for $t = 0.5$ and $t = 0.75$ are almost, but not exactly, mirror images of those at $t = 0.0$ and $t = 0.25$, respectively. This near-symmetry occurs because the sinusoidal tidal current has a period of 1 nondimensional unit. However, nonlinear effects prevent exact similarity. At $t = t_o + 0.5$, the tidal currents are the reverse of those at $t = t_o$, as are the wave patterns. For completeness, nevertheless, we will present wave patterns for an entire period.

3.1.1. Barotropic Mode (Mean Flow)

[20] The basic response obtained from the numerical experiments is that of the formation of a Taylor column having one or more modes in the horizontal, with modifications in the vertical arising from the stratification. These

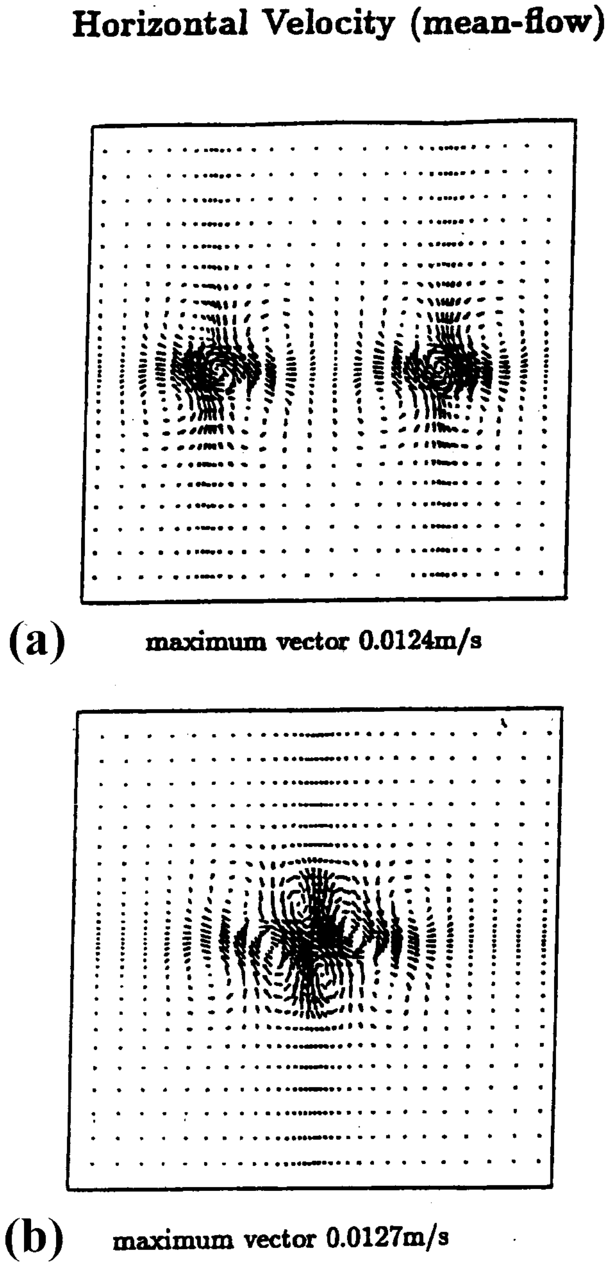

Figure 4. Barotropic mode (mean flow). (a) Two seamounts far apart; incoming tidal currents are along their common axis. (b) Two seamounts close to each other; incoming tidal currents are along their common axis.

can be termed a "Taylor cone", having multiple morphology. The response induced by tidal currents flowing over the seamounts appears in the form of a dipole. When the two seamounts are well separated, little interaction between the two dipoles is seen. Thus, in case a, there are two pairs of vortices around each seamount, rotating counterclockwise around the seamounts as seen in Figure 4a. The rotation of the dipoles is due to the tidal oscillation. As discussed above, wave patterns at t = 0.5 and t = 0.75 are mirror images of those at t = 0 and t = 0.25, respectively. (There are some minor differences in the patterns at t = 0 compared with those at t = 0.5. These differences indicate that the solutions are not completely periodic in time because a mean flow is generated through nonlinear effects.) As the distance between the two seamounts is reduced, these two pairs of vortices interact with each other, as seen in Figure 4b, case b. As a result of the interaction, the vortices merge and become basically a single dipole. At t = 0, the downstream cyclonic vortex of the right seamount and the upstream anticyclonic vortex of the left seamount appear to cancel each other, resulting in the appearance of two, remaining, tiny vortices. However, the anticyclonic vortex upstream of the seamount pair and the cyclonic vortex downstream of the seamount pair intensify. In fact, the mean flow maximum is about 60% larger than that in case a. At t = 0.25, the two anticyclonic vortices north of the seamounts merge into a single vortex, which is about 60% stronger than the single vortex in case a. Although these two pairs of vortices lose their identity in the mean flow pattern, their existence can be clearly verified in the differential field as discussed in the next section.

3.1.2. Baroclinic Structure

[21] In stratified oceans, Taylor cones/internal waves generated by bottom topography are bottom-trapped. Consequently, these waves may have no surface manifestations. However, if the vertical density gradient has a noticeable subsurface maximum, the internal wave field generated by tidal currents will have a subsurface maximum, too. This subsurface maximum could be weaker than that at the bottom; nevertheless, this local maximum is particularly interesting because of the possibility that it could result in the formation of patterns on the ocean surface that could be observed by radar. Therefore, in the following discussion of the vertical structure of the wave fields we will present the pattern at the sea surface, which corresponds to the surface and subsurface maximum. The maximum at the bottom will not be presented here because that structure is similar to the subsurface structure, although much stronger.

[22] For comparison with radar observation, it is necessary to examine the strain rate field generated by the internal waves, because (as discussed above) the strain rate provides a useful metric for inferring what can be observed in radar imagery of the ocean surface. Strain rate is defined as the sum of the spatial derivatives of the two horizontal velocity components, $\partial_x(u + v) + \partial_y(u + v)$. In case a, the strain rate pattern consists of two separated dipoles, as shown in Figure 5a. However, these strain dipoles do not seem to rotate around the seamounts. Instead, their patterns remain the same for t = 0 and t = 0.25. During the second half of the tidal period, the patterns also look similar, but their signs are opposite. In case b there are two closed dipoles, one on top of each seamount as shown in Figure 5b. (At t = 0.25, one of these dipoles is not quite well defined.) The dipoles evolve in time in case a in a similar way. The major

Figure 5. (opposite) The strain rates ($\Sigma_j \partial_{x_i} u_j$) at the sea surface, where u is the local horizontal velocity. Solid lines represent positive values and dashed lines represent negative values. (a) Two seamounts far apart; incoming tidal currents are along their common axis. (b) Two seamounts close to each other; incoming tidal currents are along their common axis.

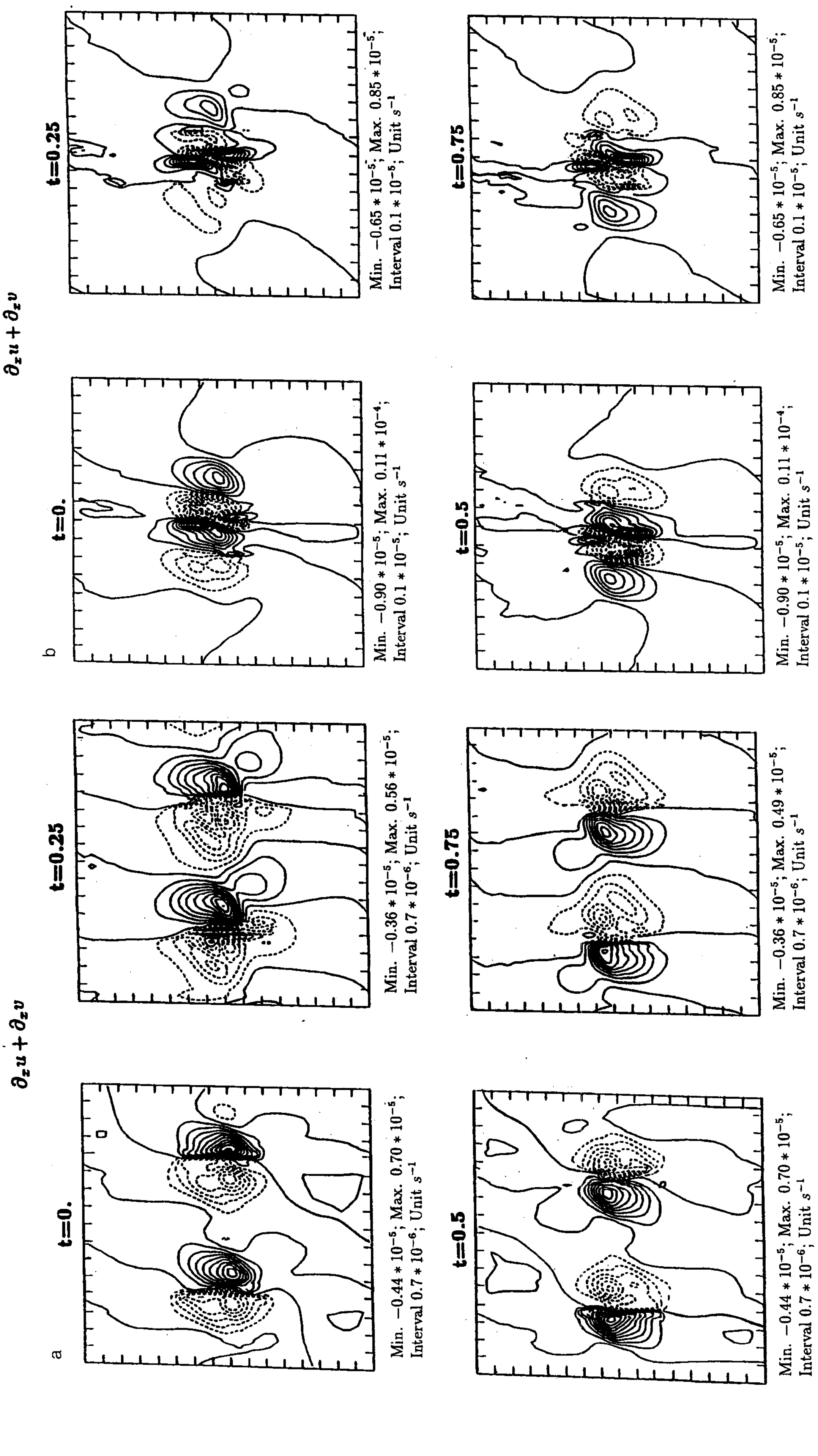
a
t=0.
Min. −0.44 * 10^-5; Max. 0.70 * 10^-5; Interval 0.7 * 10^-6; Unit s^-1
t=0.25
Min. −0.36 * 10^-5; Max. 0.56 * 10^-5; Interval 0.7 * 10^-6; Unit s^-1
t=0.5
Min. −0.44 * 10^-5; Max. 0.70 * 10^-5; Interval 0.7 * 10^-6; Unit s^-1
t=0.75
Min. −0.36 * 10^-5; Max. 0.49 * 10^-5; Interval 0.7 * 10^-6; Unit s^-1
b
t=0.
Min. −0.90 * 10^-5; Max. 0.11 * 10^-4; Interval 0.1 * 10^-5; Unit s^-1
t=0.25
Min. −0.65 * 10^-5; Max. 0.85 * 10^-5; Interval 0.1 * 10^-5; Unit s^-1
t=0.5
Min. −0.90 * 10^-5; Max. 0.11 * 10^-4; Interval 0.1 * 10^-5; Unit s^-1
t=0.75
Min. −0.65 * 10^-5; Max. 0.85 * 10^-5; Interval 0.1 * 10^-5; Unit s^-1

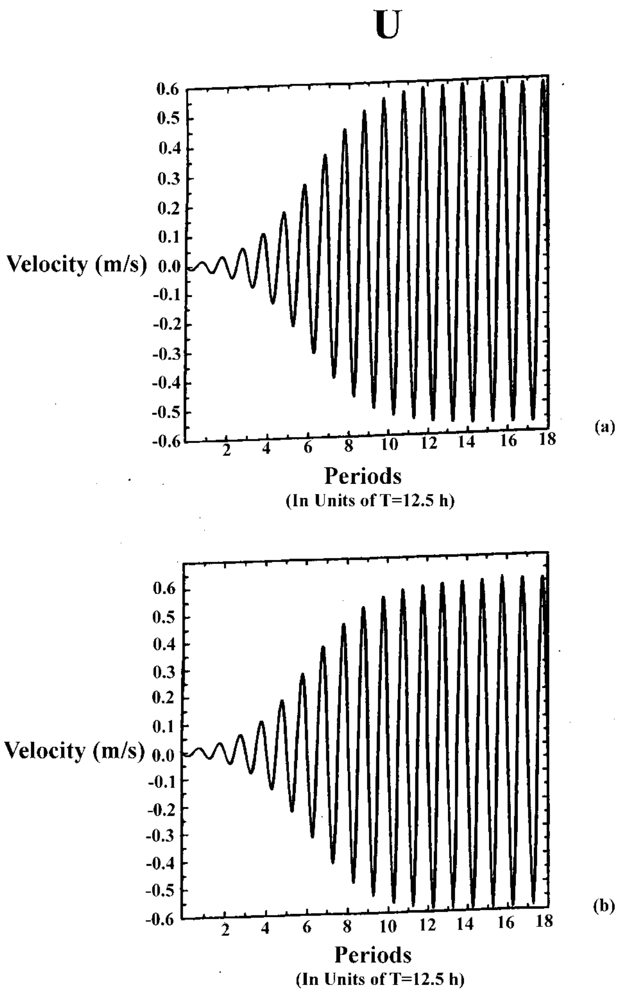

Figure 6. Time series of horizontal velocity (u) over the top of the left seamount for depths of 4300 m and 10 m. (a) Two seamounts far apart. (b) Two seamounts close to each other.

difference between the two cases is again the existence of a quadrupole in the middle. The shape of this quadrupole does not change with time. Most importantly, the maximum strain rate appears within this quadrupole. In fact, the maximum strain rate reaches 1.1×10^{-5} s^{-1} at the tidal minimum in case b. Thus, the strain rate in case b is about 60% higher than that in case a. However, based on the Relaxation Model, the strain rates in Figure 5b are still 2 orders of magnitude too small to be observed [*Gasparovic et al.*, 1988; *Thompson*, 1988; *Thompson et al.*, 1988].

[23] The situation in which the incoming tidal currents are perpendicular to the common axis of the two seamounts is similar to case b with respect to the vertical vorticity or strain rate. This situation is not shown in this study.

[24] Figures 6a and 6b show the time series of horizontal velocity (u) over the top of the left seamount at 4300 m and 10 m below the sea surface for cases a and b, respectively. Two points are worth noting: First, the horizontal velocity has approximately the same amplitude in both cases. Second, the time series of u is shifted toward positive values in both cases. Thus, there is a net positive flow, but it is more than 1 order of magnitude smaller than the instantaneous velocities. The amplitude of the horizontal velocity time series in case b is about 20% greater than in case a, but this is an order-of-magnitude estimate because it is derived from information obtained at only one fixed point.

3.2. Numerical Results from the Coupled Wave-Current Model

[25] Figure 7 is the initial spectrum, plotted in the angle-frequency coordinate plane. When the angle is 7, the spectrum propagates toward the south, with a peak frequency of 0.09 Hz, and the maximum energy density is 13.9 m^2/Hz/rad. Figure 8 shows the energy density spectrum fluctuation from the coupled wave-current model when the two seamounts are close to each other and the tidal current is directed along the common seamount axis; two model results are shown: (1) a model by WAM [*Komen et al.*, 1994] and (2) a new coastal wave model [*Lin and Huang*, 1996a, 1996b; *Lin and Perrie*, 1997, 1999]; two cases are shown: case a, when two seamounts are far apart, and case b, when two seamounts are close to each other. Figure 8a

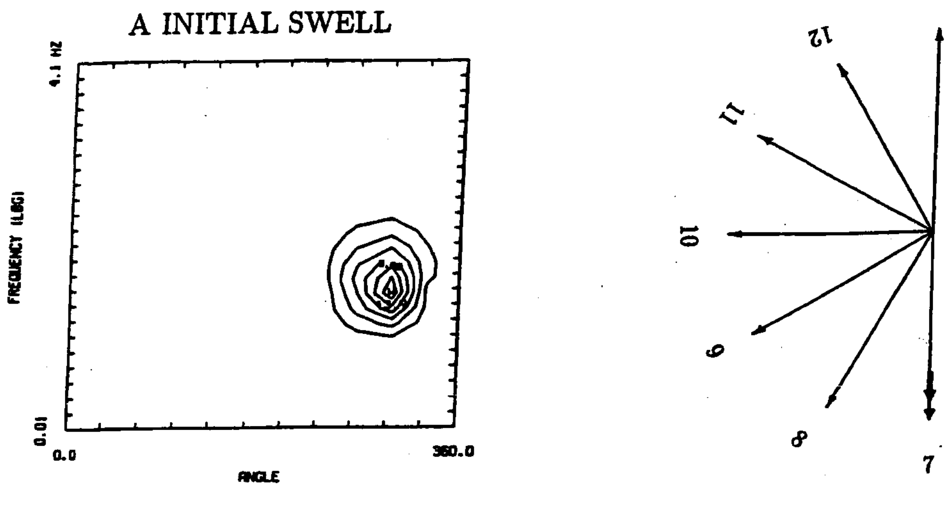

Figure 7. Initial swell in the angle-frequency coordinate. Toward the south is angle number 7.

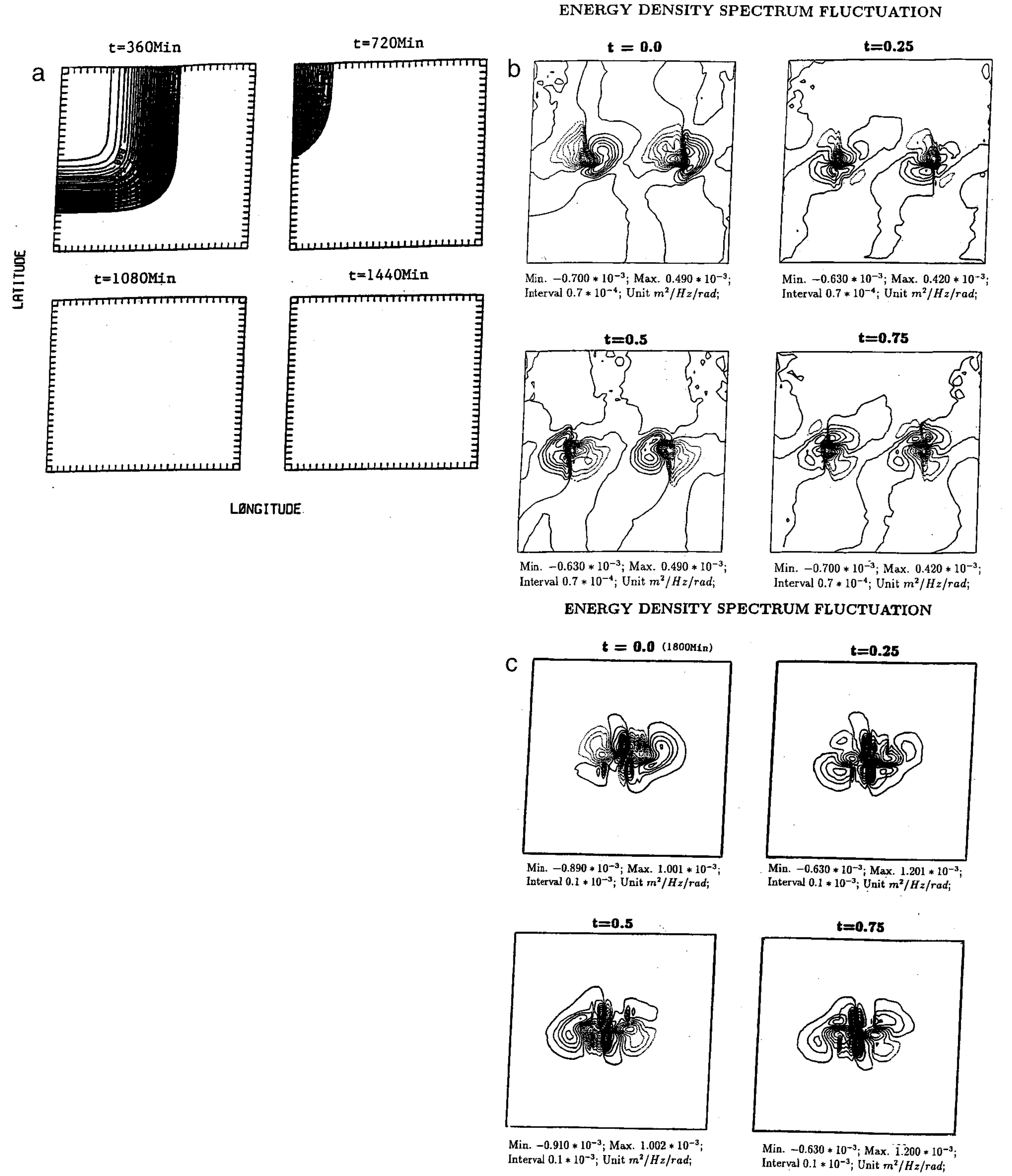

Figure 8. Coupled wave-current model results show the energy density spectrum fluctuation of sea surface when incoming tidal currents are along their common axis. Solid lines represent positive values and dashed lines represent negative values. (a) WAM. (b, c) A New Coastal Wave Model. Figure 8b shows two seamounts that are far apart, and Figure 8c shows two seamounts that are close to each other.

shows no pattern at all after the swell passes through the seamount area; that is, the entire area remains at a constant wave height in each frequency and direction. This occurs in the associated WAM model, where wave-current interaction is included indirectly, through a parameterized calculation, using an energy transfer equation.

[26] The situation is very different when the NCWM is used. This is shown in Figures 8b and 8c. Here, in

particular, dipoles are found that are very similar to those obtained in Figure 5; one appears on top of each seamount, as shown in Figures 8b and 8c. The major difference between the results shown in this figure and those found in Figure 5 is that the surface roughness in Figures 8b and 8c leads to strain rates that are about 2 orders of magnitude greater than those associated with Figure 5. Thus, in the coupled wave-current model, sea surface roughness increases by about 2 orders of magnitude. This occurs in the coupled wave-current model through wave-current interactions that lead to the formation of surface waves that result from the maximum seamount trapped wave amplitude moving from beneath the thermocline to the sea surface. The energy density fluctuations in Figure 8b are smaller than those in Figure 8c because those in Figure 8c include the nonlinear interaction between two seamount trapped waves, which are consistent with Figures 5a and 5b. Consistent with the findings of *Cooper et al.* [2000], the larger strain rates associated with Figure 8c imply that the resulting enhancements in radar modulation amplitude should be detectable at moderate angles of incidence (between 30° and 60°) either under mild wind conditions (less than 1 m/s), where the dominant electromagnetic scattering is provided by resonant Bragg waves (as in the Relaxation Model), or under stronger wind conditions (greater than 6 m/s), where wave breaking effects become important.

4. Conclusions

[27] A current response 4 times greater than the driving tidal current has been found when the semidiurnal tide is incident on a small seamount in the deep ocean. This current is generated by a resonance with seamount-trapped waves. Because of the strong vertical stratification near the sea surface (-100 m) in the northwest Pacific Ocean during the summer, the largest amplitude internal currents are found beneath the thermocline. The coupled wave-current model results show that these waves modulate the sea surface and should be observable along the tidal direction from satellite and aircraft imaging radars when two seamounts are close to each other as well as under alternative conditions, such as during periods of mild winds or in the presence of wave breaking. This is because the energy density spectrum fluctuations are about 10^{-3} m^2/Hz/rad. The strain rates associated with sea surface roughness of the uncoupled current model are 2 orders of magnitude too small to account for significant radar intensity modulation, except under extraordinary circumstances. However, the comparable strain rates associated with surface roughness of the coupled wave-current model should result in detectable radar intensity modulations that are compatible with the findings obtained from SAR imagery, obtained by the Kosmos-1870 satellite. The enhancement in strain rate that occurs in the coupled model is not due to the current model accuracy. (The current model by *Haidvogel and Aike* [1999] is an advanced current model, and is well tested.) Because the enhancement occurs primarily through wave-current interaction, to understand the origin of the enhancement, wave-current interaction must be treated accurately. In particular, as a consequence of wave-current interaction, surface waves are generated with the maximum seamount trapped wave being brought from beneath the thermocline to the sea surface. Furthermore, when the two seamounts are directly in contact, as seen in case b, the amplitude of the instantaneous internal currents and the mean-flow increases by about 60%. This nonlinear interaction between seamounts greatly increases the possibility of observing internal waves by radar. In addition, nonlinear interactions also cause the internal current patterns to become shorter in the direction transverse to the tidal direction.

[28] **Acknowledgments.** We would like to thank R. X. Huang, D. R. Thompson, R. D. Chapman, D. G. Sibeck, K. Hedstrom, A. V. Smirnov, and V. S. Etkin for their helpful discussions and suggestions and J. Apel for suggesting that we investigate this problem. The work has been supported by grants from the Office of Naval Research (ONR) under the David Taylor, Research Director, ILIR project, and through the ONR-sponsored Physics of Coastal Remote Sensing, Accelerated Research Initiative, managed by R. Mied of the Naval Research Laboratory.

References

Bell, T. H., A. B. Mays, and W. P. DeWitt, *A Compilation of Density and Brunt-Väisälä Frequency Distributions for the Upper 500 m of the World Ocean*, vol. II, *Tables*, Naval Res. Lab., Washington, D. C., 1974.

Brink, K. H., The effect of stratification on seamount-trapped waves, *Deep Sea Res.*, *36*, 825–844, 1988.

Chapman, D., Enhanced subinertial diurnal tides over isolated topographic features, *Deep Sea Res.*, *36*, 815–824, 1989.

Chelomei, V. N., et al., Studies of the sea surface using the Kosmos-1870 High-Resolution Radar, *Sov. J. Remote Sens.*, *8*(2), 306–321, 1990.

Cooper, A. L., S. R. Chubb, M. A. Sletten, and C. L. Trump, On the origin of bright lines and other features in X-band radar imagery of frontal surface velocity fields, in *Proceedings of 2000 International Geoscience and Remote Sensing Symposium (IGARSS'00)*, vol. III, pp. 1286–1288, Honolulu, Hawaii, 2000.

Gasparovic, R. F., J. R. Apel, and E. S. Kasischke, An overview of the SAR internal wave signature experiment, *J. Geophys. Res.*, *93*, 12,304–12,316, 1988.

Haidvogel, D., and B. Aike, *Numerical Ocean Circulation Modeling*, 318 pp., World Sci., River Edge, N. J., 1999.

Jensen, R., D. Resio, R.-Q. Lin, G. Van Vledder, T. Herbers, and B. Tracy, A Report of the international competition in nonlinear source function simulation in ONR held base enhancement wave prediction, report, Off. of Naval Res., Washington, D. C., 1998.

Komen, G. J., L. Cavaleri, M. Donelan, K. Hasselmann, S. Hasselmann, and P. A. E. M. Janssen, *Dynamics and Modelling of Ocean Waves*, 532 pp., Cambridge Univ. Press, New York, 1994.

Lin, R.-Q., and N. Huang, The Goddard Coastal Wave Model I, Numerical method, *J. Phys. Oceanogr.*, *26*, 833–847, 1996a.

Lin, R.-Q., and N. Huang, The Goddard Coastal Wave Model, I, Kinematics, *J. Phys. Oceanogr.*, *26*, 848–862, 1996b.

Lin, R.-Q., and W. Perrie, A new coastal wave model, III, Nonlinear wave-wave interaction, *J. Phys. Oceanogr.*, *27*, 1813–1826, 1997.

Lin, R.-Q., and W. Perrie, Wave-wave interactions in finite depth water, *J. Geophys. Res.*, *104*, 11,193–11,213, 1999.

Thompson, D. R., Calculation of radar backscatter modulations from internal waves, *J. Geophys. Res.*, *93*, 12,371–12,380, 1988.

Thompson, D. R., B. L. Gotwols, and R. E. Sterner II, A comparison of measured surface wave spectral modulations with predictions from a wave-current interaction model, *J. Geophys. Res.*, *93*, 12,339–12,343, 1988.

Zhang, X., and D. L. Boyer, Current deflections in the vicinity of multiple seamounts, *J. Phys. Oceanogr.*, *8*, 1122–1138, 1991.

S. R. Chubb, Remote Sensing Division, Code 7252, Naval Research Laboratory, 4555 Overlook Avenue, SE, Washington, D. C. 20375-5351, USA. (scott.chubb@nrl.navy.mil)

R.-Q. Lin, Department of Seakeeping, David Taylor Model Basin, Carderock, 9500 MacArthur Boulevard, West Bethesda, MD 20817-5700, USA. (linrq@nswccd.navy.mil)